

# Effective buoyancy at the surface and aloft

Nadir Jeevanjee<sup>a,b,\*</sup> and David M. Romps<sup>b,c</sup>

<sup>a</sup>Department of Physics, University of California at Berkeley, USA

<sup>b</sup>Climate and Ecosystem Sciences Division, Lawrence Berkeley National Laboratory, CA, USA

<sup>c</sup>Department of Earth and Planetary Sciences, University of California at Berkeley, USA

\*Correspondence to: N. Jeevanjee, Department of Physics, UC Berkeley, 366 LeConte Hall MC 7300, Berkeley, CA 94720, USA. E-mail: jeevanje@berkeley.edu

It is shown here that a wide, buoyant parcel of air at the surface accelerates far less rapidly than it does aloft. In particular, analytical formulae are derived for the effective buoyancy (i.e. the net vertical acceleration due to parcel buoyancy and environmental response) of idealized cylinders of diameter  $D$  and height  $H$ , located in free space and at the surface. These formulae quantify the decrease of effective buoyancy with increasing aspect ratio  $D/H$ , and show that this effect is more pronounced for surface cylinders, especially when  $D/H > 1$ . We gain intuition for these results by considering the pressure fields generated by these buoyant parcels, and we test our results with large-eddy simulations. Our formulae can inform parametrizations of the vertical velocity equation for clouds, and also provide a quantitative map of the ‘grey zone’ in numerical modelling between hydrostatic and non-hydrostatic regimes.

*Key Words:* buoyancy; convection; Archimedean buoyancy; effective buoyancy; large-eddy simulations

Received 3 June 2015; Revised 15 September 2015; Accepted 28 September 2015; Published online in Wiley Online Library 23 November 2015

## 1. Introduction

The Archimedean buoyancy in the anelastic approximation is given by

$$B \equiv -g \frac{\rho'}{\bar{\rho}} \quad (1)$$

where  $g$  is the gravitational acceleration,  $\bar{\rho}(z)$  is a reference density profile, and the density  $\rho$  is decomposed as  $\rho = \bar{\rho} + \rho'$ . It is the driving force behind thermal convection, but is also an incomplete and somewhat unsatisfactory measure of buoyant acceleration since, in general, the Lagrangian vertical acceleration  $dw/dt$  does not equal  $B$ , even when the atmosphere is initially motionless. This is because the acceleration of a buoyant parcel necessarily produces a back-reaction from the environment, which must move out of the way to accommodate the parcel's motion. This back-reaction is given (in the anelastic approximation) by the gradient of the buoyancy pressure perturbation  $p'_b$ , which is defined as the solution to the Poisson equation\*

$$-\nabla^2 p'_b = -\partial_z(\bar{\rho}B) \quad (2)$$

(cf. Markowski and Richardson, 2011, p.28). The vertical accelerations  $B$  and  $-(\partial_z p'_b)/\bar{\rho}$  are thus inseparable, which has led some authors to consider only their combination  $B - (\partial_z p'_b)/\bar{\rho}$  in their analyses (e.g. Krueger *et al.*, 1996; Xu and Randall, 2001;

Davies-Jones, 2003; Torri *et al.*, 2015). Such an approach was expressly advocated by Doswell and Markowski (2004), who also argue that  $B - (\partial_z p'_b)/\bar{\rho}$  is independent of reference density  $\bar{\rho}$ , resolving another deficiency of Eq. (1).

While focusing on  $B - (\partial_z p'_b)/\bar{\rho}$  is sensible, this quantity, which we refer to as the ‘effective buoyancy’  $\beta$  following Davies-Jones (2003), has been relatively little studied as an object in its own right. Previous studies and textbook treatments have largely focused on  $\nabla p'_b$  (e.g. Yau, 1979; Markowski and Richardson, 2011; Houze, 2014), though there are exceptions which we will discuss below (Pauluis and Garner, 2006; Nugent and Smith, 2014). Parametrizations of the vertical velocity equation employed in convection schemes usually strive to account for effective buoyancy via a ‘virtual mass’ coefficient, but its value is rather uncertain (de Roode *et al.*, 2012). Finally, there are surface effects which are significant but rarely quantified. We illustrate these in Figure 1, which shows  $x$ – $z$  cross-sections at  $y = 0$  of  $B$  and  $\beta$  for Gaussian density bubbles of the form

$$\rho(\mathbf{x}) = \bar{\rho}(z) + \Delta\rho \exp \left\{ -\frac{r^2}{R^2} - \left( \frac{z - z_{\text{cm}}}{H/2} \right)^2 \right\}, \quad (3)$$

with height  $H = 1000$  m, radius  $R = 1000$  m,  $\Delta\rho = -\bar{\rho}(z_{\text{cm}})/300$  for an approximate temperature anomaly of 1 K, and bubble centres  $z_{\text{cm}} = 2000, 500, \text{ and } 0$  m.<sup>†</sup> The ratio of the maximum of  $\beta$  to the maximum of  $B$  is roughly 1/2 for the ‘free’

\*This equation just says that the divergence of  $-\nabla p'_b$  must cancel the divergence generated by  $\bar{\rho}Bz$ , a requirement imposed by anelastic mass continuity.

<sup>†</sup>The domain set-up and  $\bar{\rho}(z)$  for the bubbles is the same as for the large-eddy simulations discussed in section 5 below, and we compute  $\beta$  numerically as in Jeevanjee and Romps (2015).

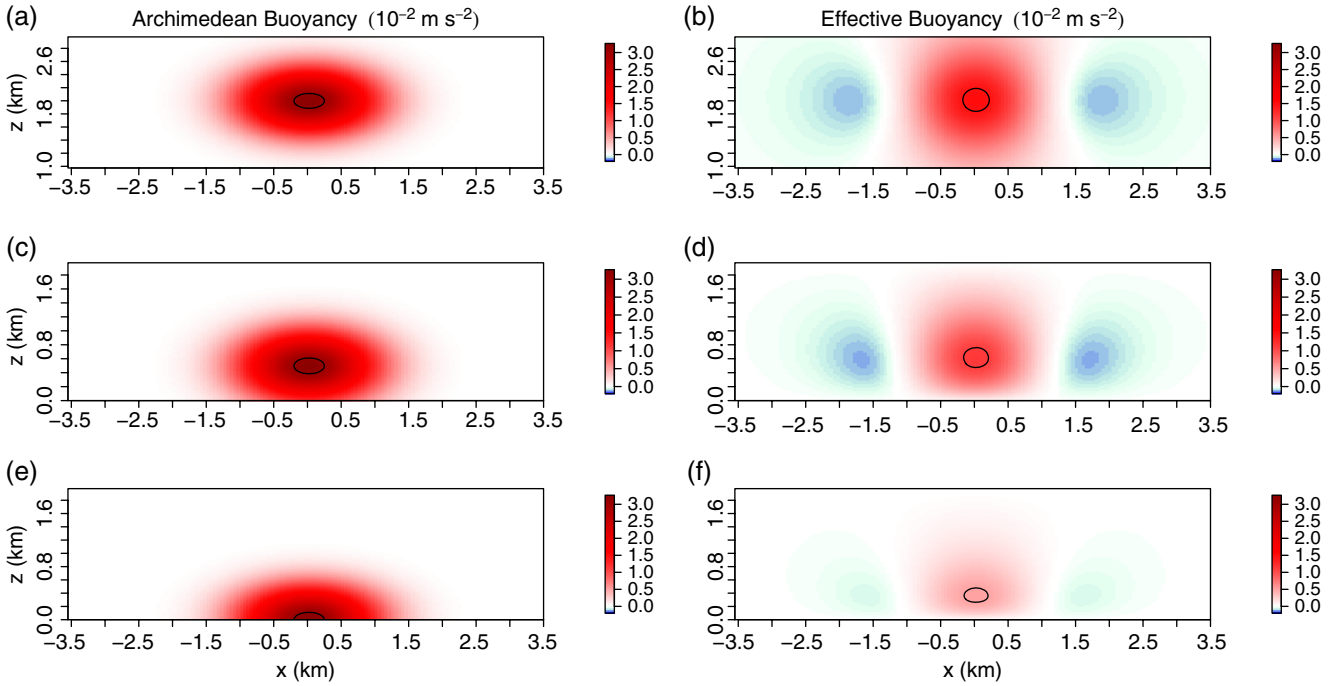


**Figure 1.**  $x$ - $z$  cross-sections at  $y = 0$  of (a,c,e) Archimedean buoyancy  $B$  and (b,d,f) effective buoyancy  $\beta = B - (\partial_z p'_b)/\bar{\rho}$  (both  $10^{-2} \text{ m s}^{-2}$ ) for Gaussian bubbles of the form Eq. (3) with  $R = 1000 \text{ m}$ ,  $H = 1000 \text{ m}$ , and centre height  $z_{\text{cm}}$  of (a,b) 2000 m, (c,d) 500 m, and (e,f) 0 m. Horizontal and vertical dimensions are plotted to scale, though the vertical axes in (a,b) differ from those of (c-f), and the contour is drawn at the 95th percentile value in each plot. Note the marked difference in magnitude between  $B$  and  $\beta$ , how this difference becomes more pronounced as the bubble moves toward the surface, and how the maximum of  $\beta$  stays a finite height above the surface even as the maximum of  $B$  approaches  $z = 0$ .

bubble, and this ratio decreases rapidly as the bubble approaches the surface. At the surface one can also see that the maxima of  $\beta$  and  $B$  are no longer co-located.

At present, we have little quantitative or even qualitative understanding of such behaviour. We aim to remedy this by developing and testing analytical expressions for the effective buoyancy of fluid parcels near the surface and aloft. We will solve the Poisson equation for  $\beta$  given in Davies-Jones (2003) (hereafter DJ03) for idealized density distributions, and employ the closely related ‘buoyancy pressure’ introduced by Jeevanjee and Romps (2015, hereafter JR15) to gain intuition for our results.

## 2. Preliminaries

### 2.1. The Poisson equation for effective buoyancy

As in JR15, we begin by defining effective buoyancy  $\beta$  as the Lagrangian vertical acceleration that would result from zeroing out the wind fields:

$$\beta \equiv \left. \frac{dw}{dt} \right|_{\mathbf{u}=0}. \quad (4)$$

If one starts with the usual approximation of the anelastic equation of motion in the absence of viscous and Coriolis forces (Emanuel, 1994, p. 11),

$$\frac{d\mathbf{u}}{dt} = B\hat{\mathbf{z}} - \frac{1}{\bar{\rho}}\nabla p',$$

where  $p' = p - \bar{p}$  is the perturbation pressure and  $\bar{p}$  is a reference pressure profile in hydrostatic balance with  $\bar{\rho}$ , then it is straightforward to show that  $\beta = B - (\partial_z p'_b)/\bar{\rho}$ , where  $p'_b$  satisfies Eq. (2). If, however, one follows DJ03 and Das (1979) and defines a *locally* hydrostatic pressure field

$$p_{\text{hyd}}(x, y, z) \equiv g \int_z^\infty \rho(x, y, z') dz'$$

and corresponding non-hydrostatic pressure field  $p_{\text{nh}} \equiv p - p_{\text{hyd}}$ , then one obtains an alternate form of the anelastic momentum equation

$$\bar{\rho} \frac{d\mathbf{u}}{dt} = -\nabla p_{\text{nh}} - \nabla_h p_{\text{hyd}}, \quad (5)$$

where  $\nabla_h \equiv \partial_x \hat{\mathbf{x}} + \partial_y \hat{\mathbf{y}}$ . It is then straightforward to apply the definition (4) to obtain the following simple Poisson equation for  $\beta$ , due to DJ03:

$$-\nabla^2(\bar{\rho}\beta) = g\nabla_h^2 \rho. \quad (6)$$

(Here,  $\nabla_h^2 \equiv \partial_x^2 + \partial_y^2$ , and the difference between  $\nabla_h^2$  and  $\nabla^2$  is the source of all the interesting physics that follows.) Neglecting vertical variations in  $\bar{\rho}$  (since the scale of such variations is larger than the density anomalies we will consider) and noting that  $\nabla_h^2 \rho = \nabla_h^2 \rho'$ , we obtain an even simpler form,

$$-\nabla^2 \beta = -\nabla_h^2 B. \quad (7)$$

This is the Poisson equation for  $\beta$  that we will use in this article.

### 2.2. Effective buoyancy and the buoyancy pressure

Though Eq. (7) is all we require to obtain analytical expressions for  $\beta$ , getting intuition for what these expressions tell us will require us to consider the *buoyancy pressure*  $p_\beta$ , first introduced in JR15. Analogous to the definition (4),  $p_\beta$  is defined as the non-hydrostatic pressure that would result from zeroing out the wind fields:

$$p_\beta \equiv p_{\text{nh}} \Big|_{\mathbf{u}=0}.$$

Taking the divergence of Eq. (5), invoking anelastic mass continuity, and setting  $\mathbf{u} = 0$  yields the Poisson equation

$$-\nabla^2 p_\beta = \nabla_h^2 p_{\text{hyd}}. \quad (8)$$

This equation just says that the divergence of  $-\nabla p_\beta$  must cancel out any divergence produced by the horizontal hydrostatic

pressure gradient  $-\nabla_h p_{\text{hyd}}$ . That Eq. (8) is reminiscent of Eqs (6) and (7) is no accident; applying  $-\partial_z$  to both sides of Eq. (8) yields  $-\nabla^2(-\partial_z p_\beta) = g\nabla_h^2 \rho$ , and it follows from Eq. (5) that the boundary conditions of  $-\partial_z p_\beta$  are identical to that of  $\bar{\rho}\beta$ , so we conclude that

$$\bar{\rho}\beta = -\partial_z p_\beta. \tag{9}$$

Thus,  $\beta$  is essentially the vertical component of the pressure gradient  $-\nabla p_\beta$  which arises to compensate for hydrostatic pressure forces. Considering  $p_\beta$  will give us a picture of the full 3D circulation resulting from parcel buoyancy, which will facilitate intuition for  $\beta$ .

### 2.3. Back-of-the-envelope estimate of effective buoyancy

We will be interested in solutions of Eq. (7) for parcels of characteristic height  $H$  and horizontal scale  $D$ . In terms of these parameters, we can roughly estimate  $\partial_r^2 \sim 1/D^2$  (here and below,  $r \equiv \sqrt{x^2 + y^2}$  is our cylindrical radial coordinate) and  $\partial_z^2 \sim 1/H^2$  and plug into Eq. (7) to obtain

$$\beta = \frac{B}{1 + D^2/H^2}. \tag{10}$$

This suggests that  $|\beta| < |B|$ , as we expect, and that the proportionality factor depends quadratically on a parcel's aspect ratio  $D/H$ . The exact solutions of Eq. (7) for isolated cylindrical density anomalies, which we will present below, confirm this.

Before proceeding to that analysis, let us use Eq. (10) to re-do the usual linear perturbation analysis of a parcel in a stratified environment with potential temperature profile  $\theta(z)$  and Brunt-Väisälä frequency  $N = \sqrt{g d(\ln \theta)/dz}$ . In the linear regime with no background flow, there is no 'inertial' or 'dynamic' pressure stemming from the nonlinear advection term in the momentum equation, and so  $dw/dt = \beta$  (Jeevanjee and Romps, 2015). Applying this to a small displacement  $\delta z$ , and using Eq. (10), we then have

$$\frac{d^2 \delta z}{dt^2} = -\frac{N^2}{1 + D^2/H^2} \delta z.$$

Letting  $k \equiv 1/D$  and  $m \equiv 1/H$ , this implies that the parcel will oscillate with angular frequency

$$\omega = \frac{N}{\sqrt{1 + D^2/H^2}} = \frac{Nk}{\sqrt{k^2 + m^2}},$$

which is just the usual expression for the frequency of a gravity wave with horizontal and vertical wavenumbers  $k$  and  $m$ . Thus, the reduction of the gravity-wave frequency from the Brunt-Väisälä value can be seen as just the effect of effective buoyancy. That Eq. (10) gives the exact right answer for  $\omega$  is no accident, as Eq. (10) is itself exact for gravity waves, as can be checked by plugging in oscillating fields  $B, \beta \sim \exp\{i(kx + mz - \omega t)\}$  into Eq. (7).

Despite the applicability of Eq. (10) in the gravity-wave context, and the fact that it captures the reduction of  $\beta$  relative to  $B$  as a function of a parcel's aspect ratio, it is just a crude estimate and does not capture the dependence of  $\beta$  on a parcel's proximity to the surface seen in Figure 1. To make further progress, we will need the exact solutions presented in the next two sections.

### 3. The free cylinder

We now refine the result (10) for the case of a 'free' parcel, i.e. a density anomaly in an infinite domain without boundary. The case of a parcel at the surface is treated in the next section. We proceed by partially solving the Poisson equation (7) for a uniform cylindrical density anomaly centred around the origin

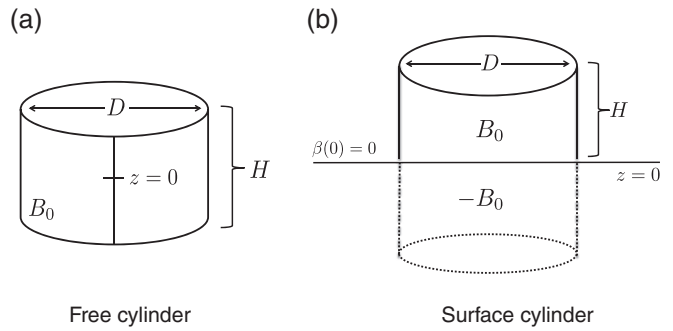


Figure 2. Illustrations of the buoyancy distributions appearing on the right-hand side of Eq. (7) for (a) the free cylinder and (b) the surface cylinder. The distribution is even about  $z = 0$  for the free cylinder, but odd for the surface cylinder, enforcing a  $\beta(0) = 0$  boundary condition for the latter.

with Archimedean buoyancy  $B_0$ , diameter  $D$ , and height  $H$ . This is illustrated in Figure 2(a). The buoyancy field thus has the form

$$B = B_0 \mathcal{H}\left(\frac{D}{2} - r\right) \mathcal{H}\left(z + \frac{H}{2}\right) \mathcal{H}\left(\frac{H}{2} - z\right), \tag{11}$$

where the Heaviside step functions  $\mathcal{H}$  serve to restrict the density anomaly to our cylinder. Plugging this into Eq. (7) yields

$$-\nabla^2 \beta = \frac{B_0}{r} \partial_r \left\{ r \delta\left(r - \frac{D}{2}\right) \right\} \mathcal{H}\left(z + \frac{H}{2}\right) \mathcal{H}\left(\frac{H}{2} - z\right), \tag{12}$$

where  $\delta(r) = \partial_r \mathcal{H}(r)$  is the Dirac delta function.

A complete analytical solution of Eq. (12) would be arduous, if not impossible, but here we seek only the solution for  $\beta$  on the  $z$ -axis, which simplifies the problem considerably. Since the Green's function  $G(\mathbf{x}; \mathbf{x}')$  for the Laplacian  $\nabla^2$  for a field with 'open' boundary conditions (i.e. a field which vanishes at infinity) is just  $1/(4\pi |\mathbf{x} - \mathbf{x}'|)$ , and since we are interested only in  $\mathbf{x} = (0, 0, z)$ ,  $\beta(z)$  on the  $z$ -axis is given by

$$\begin{aligned} \beta(z) &= \int d^3 \mathbf{x}' G\{(0, 0, z); \mathbf{x}'\} \nabla_h^2 B(\mathbf{x}') \\ &= \frac{B_0}{2} \int_{-H/2}^{H/2} dz' \int_0^\infty dr' \frac{\partial_{r'} \{r' \delta(r' - D/2)\}}{\sqrt{r'^2 + (z - z')^2}}. \end{aligned}$$

This double integral can be evaluated using integration by parts, the definition of the delta function, and trigonometric substitution. The result is

$$\beta(z) = \frac{B_0}{2} \left\{ \frac{1 - 2z/H}{\sqrt{D^2/H^2 + (1 - 2z/H)^2}} + \frac{1 + 2z/H}{\sqrt{D^2/H^2 + (1 + 2z/H)^2}} \right\}. \tag{13}$$

This analytical expression is one of the main results of this article.

The function  $\beta(z)$  is plotted as a function of  $z/H$  in Figure 3 for various aspect ratios  $D/H$ , which are depicted to scale by pink boxes. Note that as  $D/H$  increases, the maximum of  $\beta$  decreases. This can be further illustrated by evaluating Eq. (13) at  $z = 0$ , which yields

$$\beta(0) = \frac{B_0}{\sqrt{1 + D^2/H^2}}. \tag{14}$$

This is plotted as a function of aspect ratio in Figure 4, and quantifies the effect of aspect ratio on buoyant accelerations: for  $D/H = 1$ , the environmental response offsets the Archimedean buoyancy by 30%; for  $D/H = 2$ , 50%. For small aspect ratios  $D/H \ll 1$ , the plot of Eq. (14) in Figure 4 flattens out, so narrow plumes do not become significantly more buoyant by splitting

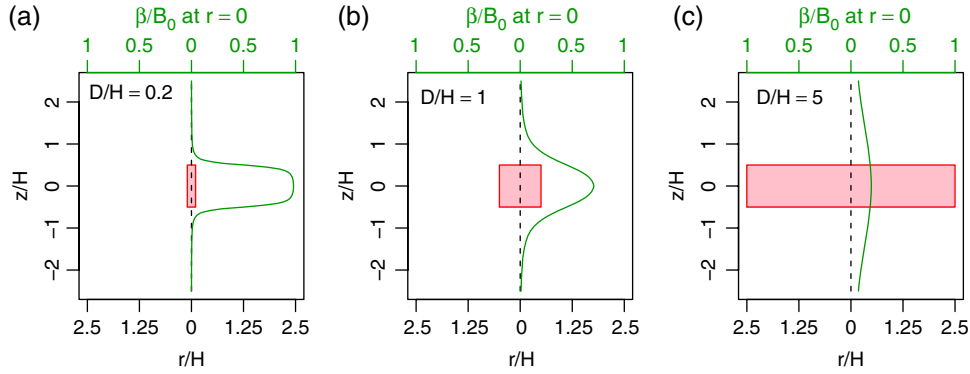


**Figure 3.** The curves  $\beta(z)$  (green) from Eq. (13) for free cylinders of aspect ratios  $D/H$  (a) 0.2, (b) 1.0, and (c) 5.0. The cylinders themselves are depicted to scale in pink. As  $D/H$  increases, there is a marked decrease in the maximum of  $\beta(z)$ , as well as an increase in the vertical scale over which  $\beta$  decays.

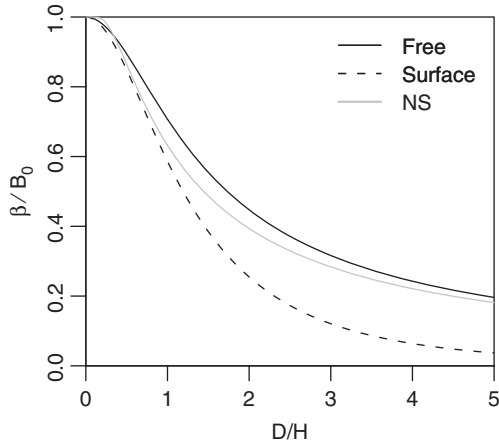


**Figure 4.** Effective buoyancies at the centre of the free cylinder (Eq. (14), solid line) and the surface cylinder (Eq. (23), dashed line) as a function of  $D/H$ . Note that  $\beta$  is always smaller for the surface cylinder than for the free one, and that it decreases much more rapidly as  $D/H$  increases. The thin grey line plots the result (29) of Nugent and Smith (2014), which tracks our Eq. (14) very closely.

apart. In this regime we can also Taylor-expand the denominator in Eq. (14) to first order which yields

$$\beta(0) \approx \frac{B_0}{1 + D^2/(2H^2)} \quad \text{when } D/H \ll 1,$$

an expression very similar to Eq. (10). For the opposite, large aspect-ratio, regime we have the alternate approximation

$$\beta(0) \approx B_0 \frac{H}{D} \quad \text{when } D/H \gg 1. \quad (15)$$

We will contrast this expression with its analogue for the surface cylinder in the next section.

These formulae quantify the decline of effective buoyancy with aspect ratio. What causes this decline, however? And why does it take the form Eq. (15) in the large-aspect-ratio limit? To answer these questions, we turn to the buoyancy pressure  $p_\beta$  introduced in section 2.2. We must first find  $p_\beta(z)$ , which is easily obtained via Eq. (9) by integrating Eq. (13). Imposing the boundary condition  $p_\beta \rightarrow 0$  as  $z \rightarrow \infty$  yields

$$p_\beta(z) = \frac{\Delta p_{\text{hyd}}}{2} \left\{ -\sqrt{D^2/H^2 + (1 - 2z/H)^2} + \sqrt{D^2/H^2 + (1 + 2z/H)^2} - 2 \right\}, \quad (16)$$

where

$$\Delta p_{\text{hyd}} \equiv -\bar{\rho} B_0 H/2 \quad (17)$$

is the  $p_{\text{hyd}}$  anomaly at the cylinder's centre. Evaluating Eq. (16) at  $z = 0$  yields

$$p_\beta(0) = -\Delta p_{\text{hyd}}. \quad (18)$$

This simple result is key for understanding the free cylinder, and does not hold for the surface cylinder. To gain intuition for it, consider a smooth, cylindrical buoyancy distribution (e.g. a Gaussian bubble as in Figure 1), as depicted schematically in Figure 5(a); the cylinder of uniform buoyancy given by Eq. (11) can be seen as a limit of such distributions. Figure 5(a) gives a heuristic derivation of Eq. (18), as follows.

1. The hydrostatic pressure anomaly  $\Delta p_{\text{hyd}} < 0$  in the cylinder drives convergence into the cylinder via  $-\nabla_h p_{\text{hyd}}$  (blue arrows).
2. This must be balanced by divergence from  $-\nabla p_\beta$ , according to Eq. (8). The  $z \rightarrow -z$  symmetry of Eq. (7) implies that  $\beta$  at cylinder top and bottom must be equal, however, so the vertical component of  $-\nabla p_\beta$  cannot contribute any divergence (vertical green arrows).
3. The horizontal divergence of  $-\nabla p_\beta$  must then balance the convergence from  $-\nabla_h p_{\text{hyd}}$  (horizontal green arrows). Since this balance occurs over a common length scale  $D$ , we can infer Eq. (18).

Now, a key feature of Eq. (18) is that  $p_\beta(0)$  is independent of horizontal scale. Why, then, does  $\beta$  decline with increasing  $D/H$  for fixed  $H$ ? As shown in the Appendix, for large aspect ratios the normalized field  $p_\beta/p_\beta(0)$  is a fixed function of  $\mathbf{x}/D$ , with negligible  $H$ -dependence. In particular, this means that the height at which  $p_\beta$  decays to a given fraction of itself scales with  $D$ . Thus,  $\beta = -(\partial_z p_\beta)/\bar{\rho}$  must scale as

$$\beta \sim \frac{p_\beta(0)}{\bar{\rho} D}. \quad (19)$$

If we combine this with Eq. (18) and the definition (17) we get

$$\beta \sim -\frac{\Delta p_{\text{hyd}}}{\bar{\rho} D} \sim B_0 \frac{H}{D}, \quad (20)$$

which is just the scaling we found in Eq. (15). Thus, the basic reason that aspect ratio matters for a free parcel is that *the vertical scale of  $p_\beta$  is a function of the parcel's horizontal scale  $D$* . (This can also be inferred from Figure 3.) If  $D$  increases while  $H$  (and hence  $p_\beta(0) = -\Delta p_{\text{hyd}}$ ) is fixed, a taller column of air must be moved with a fixed pressure differential, decreasing the gradient  $\beta = -(\partial_z p_\beta)/\bar{\rho}$ .

#### 4. The surface cylinder

We now turn to parcels located at the lower boundary of a domain, where the vertical velocity  $w$  is identically 0 and hence so

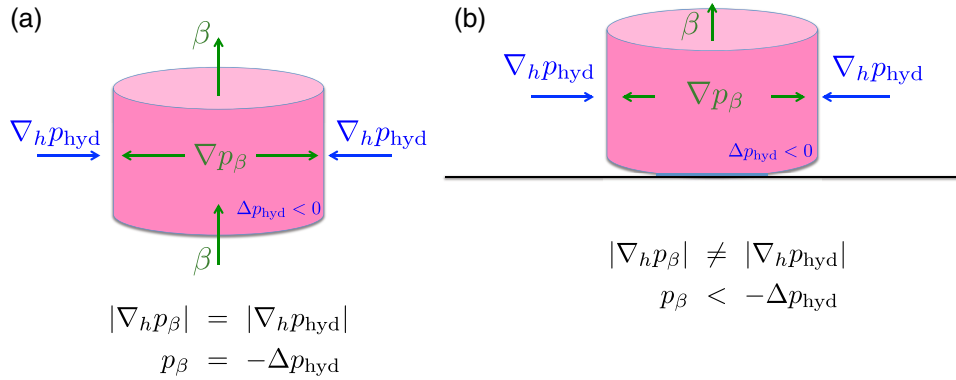


**Figure 5.** Cartoon of the gradients  $-\nabla_h p_{\text{hyd}}$  and  $-\nabla p_\beta$  and associated divergences for (a) the free cylinder and (b) the surface cylinder. Note that for the free cylinder, the vertical divergence from  $-\nabla_z p_\beta = \bar{\rho}\beta$  is 0, so the horizontal convergence from  $-\nabla_h p_{\text{hyd}}$  must be balanced entirely by horizontal divergence from  $-\nabla_h p_\beta$ , which yields  $p_\beta = -\Delta p_{\text{hyd}}$ . For the surface cylinder there is a vertical contribution to the divergence since  $\beta(0) = 0$ , and so a smaller value of  $|\nabla_h p_\beta|$  (and its divergence) is sufficient to balance the divergence from  $-\nabla_h p_{\text{hyd}}$ , yielding  $p_\beta < -\Delta p_{\text{hyd}}$ .

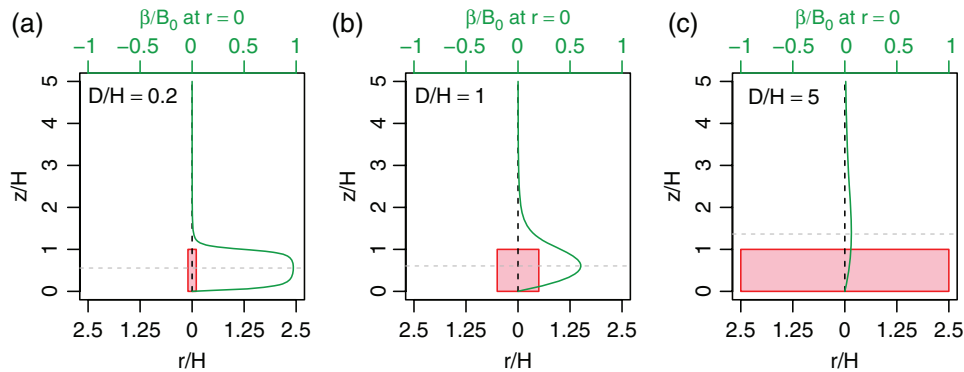


**Figure 6.** As Figure 3, but for surface cylinders with  $\beta(z)$  given by Eq. (22). In addition to a decrease in  $\beta$  and increase in vertical scale as  $D/H$  increases, the location  $z_{\text{max}}$  (light grey dashed line) of  $\beta_{\text{max}}$  moves upward, with  $z_{\text{max}}$  located just above the cylinder for  $D/H = 5$ .

is  $\beta$  by Eq. (4). To solve Eq. (7) for a cylinder at the surface (where the surface is at  $z = 0$ ), we employ the method of images (DJ03; Griffiths, 2013). The idea of this technique is to enforce a  $\beta(0) = 0$  boundary condition by solving the open boundary condition problem as in the previous section, but with an additional ‘image cylinder’ generated by reflecting the original surface cylinder across the  $z = 0$  plane and switching the sign of its anomaly (Figure 2(b)). The source term  $\nabla_h^2 B$  in Eq. (7) will then be odd with respect to  $z$ , which implies  $\beta$  will be odd too, ensuring  $\beta(0) = 0$ .

In this case, then, the Poisson equation for  $\beta$  is

$$-\nabla^2 \beta = -\nabla_h^2 B_0 \mathcal{H}(R - r) \times \{ \mathcal{H}(z)\mathcal{H}(H - z) - \mathcal{H}(-z)\mathcal{H}(H + z) \}. \quad (21)$$

Integration against the Green’s function as in the previous section yields the desired formula for  $\beta$  along the  $z$ -axis:

$$\beta(z) = \frac{B_0}{2} \left( \frac{1 - z/H}{\sqrt{D^2/4H^2 + (1 - z/H)^2}} + \frac{2z/H}{\sqrt{D^2/4H^2 + z^2/H^2}} - \frac{1 + z/H}{\sqrt{D^2/4H^2 + (1 + z/H)^2}} \right). \quad (22)$$

This expression is the other main analytical result of this article. This  $\beta(z)$  is plotted as function of  $z/H$  for various  $D/H$  in Figure 6. Similar to the free cylinder, the overall magnitude of  $\beta$  decreases with increasing  $D/H$ . To analyze this, we estimate the parcel’s overall effective buoyancy by evaluating  $\beta$  at the centre of the cylinder, yielding

$$\beta(H/2) = \frac{3B_0}{2} \left( \frac{1}{\sqrt{1 + D^2/H^2}} - \frac{1}{\sqrt{9 + D^2/H^2}} \right). \quad (23)$$

We plot this function against  $D/H$  as the dashed line in Figure 4. Note that *this curve is always less than that for the free cylinder*, consistent with Figure 1, and declines much more rapidly with increasing  $D/H$ . In fact, the large-aspect-ratio limit gives

$$\beta(0) \approx 6B_0 \frac{H^3}{D^3} \quad \text{when } D/H \gg 1, \quad (24)$$

which should be compared with the  $H/D$  scaling in Eq. (15).

Another noteworthy feature of Figure 6 is that, like the free cylinder, the vertical scale over which  $\beta$  declines increases as  $D$  increases, but in this case the location  $z_{\text{max}}$  of the maximum of  $\beta(z)$  (light grey dashed line in Figure 6) also changes, and even appears outside the cylinder for  $D/H = 5$ . This may be surprising, but is consistent with the fact that, for  $D \gg H$ ,  $z_{\text{max}}$  scales with  $D$  (Appendix).

Why do surface parcels accelerate less than free ones? As in the previous section, we turn to  $p_\beta$  for insight. Again invoking Eq. (9), we integrate Eq. (22) with our  $p_\beta \rightarrow 0$  as  $z \rightarrow \infty$  boundary condition to obtain

$$p_\beta(z) = \frac{\Delta p_{\text{hyd}}}{2} \left\{ -\sqrt{\frac{D^2}{4H^2} + \left(1 - \frac{z}{H}\right)^2} + 2\sqrt{\frac{D^2}{4H^2} + \frac{z^2}{H^2}} - \sqrt{\frac{D^2}{4H^2} + \left(1 + \frac{z}{H}\right)^2} \right\}. \quad (25)$$

Taking the  $D/H \gg 1$  limit in Eq. (25) and evaluating at  $z = 0$  then gives

$$p_\beta(0) \approx -\Delta p_{\text{hyd}} \frac{H}{D} \ll -\Delta p_{\text{hyd}}. \quad (26)$$

This stands in marked contrast to the free cylinder result (18), and is one of the main ways in which the surface cylinder differs

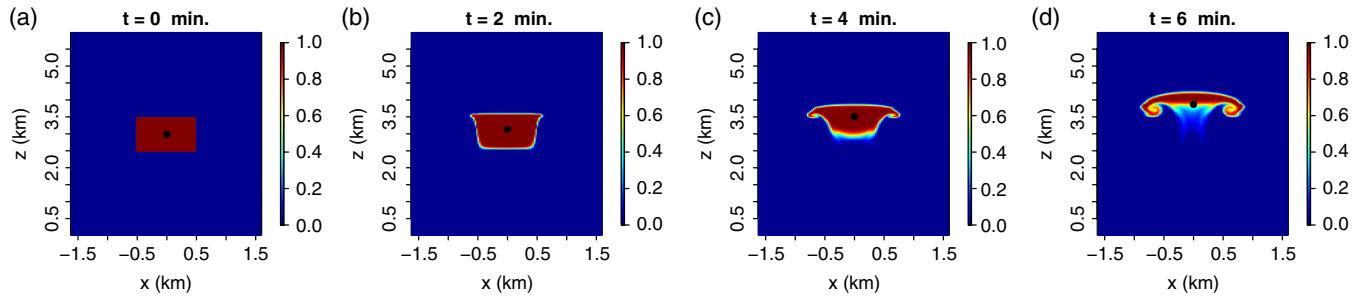


**Figure 7.**  $x$ - $z$  cross-sections at  $y = 0$  of  $q_{\text{purity}}$ , along with  $z_{\text{cm}}(t)$  (black circles) for the  $D = 1000$  m free cylinder at  $t =$  (a) 0 min, (b) 2 min, (c) 4 min and (d) 6 min. Only the middle half of the horizontal domain is shown.

from the free one. We again give a heuristic derivation for a smooth cylindrical density distribution, shown in Figure 5(b), as follows:

1. The hydrostatic pressure anomaly  $\Delta p_{\text{hyd}} < 0$  in the cylinder drives horizontal convergence into the cylinder via  $-\nabla_{\text{h}} p_{\text{hyd}}$  (blue arrows).
2. This must again be balanced by divergence from  $-\nabla p_{\beta}$ . For the surface cylinder, however, there is now a contribution from the vertical component of  $-\nabla p_{\beta}$  (vertical green arrow). This is because the  $\beta(0) = 0$  boundary condition at the surface breaks the reflection symmetry about the horizontal plane passing through the cylinder's centre.
3. The horizontal component of  $-\nabla p_{\beta}$  is thus no longer required to balance all of the convergence from  $-\nabla_{\text{h}} p_{\text{hyd}}$  (horizontal green arrows), and so can have a smaller magnitude  $|-\nabla_{\text{h}} p_{\beta}| < |-\nabla_{\text{h}} p_{\text{hyd}}|$ . Since these gradients occur over a common length scale  $D$ , we can infer  $p_{\beta}(0) < -\Delta p_{\text{hyd}}$ , as expressed in Eq. (26).

We can now combine the foregoing with our earlier results to give a heuristic derivation of the scaling in Eq. (24). We have three scaling laws concerning the effective buoyancy of a surface parcel when  $D \gg H$ :

1. From Eq. (19), we know that  $\beta_{\text{max}} \sim p_{\beta}(0)/(\bar{\rho}D)$ .
2. From Eq. (26), we know that the effect of a non-zero vertical divergence of  $-\nabla p_{\beta}$ , which arises from broken reflection symmetry, gives  $p_{\beta}(0) \sim \Delta p_{\text{hyd}}H/D$ .
3. Assuming a linear increase of  $\beta$  with height from  $z = 0$  to  $z_{\text{max}}$ , the scaling  $z_{\text{max}} \sim D$  then gives  $\beta(H/2) \sim \beta_{\text{max}}H/D$ .

Combining these three scaling laws then gives

$$\begin{aligned} \beta\left(\frac{H}{2}\right) &\sim \beta_{\text{max}} \frac{H}{D} && \text{by scaling law 3} \\ &\sim \frac{p_{\beta}(0)H}{\bar{\rho}D} && \text{by scaling law 1} \\ &\sim -\frac{\Delta p_{\text{hyd}}}{\bar{\rho}D} \frac{H^2}{D^2} && \text{by scaling law 2} \\ &\sim B_0 \frac{H^3}{D^3} && \text{by definition (17)}. \end{aligned}$$

Roughly speaking, each of our scaling laws yields a factor of  $H/D$ , combining to give a  $H^3/D^3$  scaling just as in Eq. (24).

## 5. LES tests

We now test the dependence of effective buoyancy on parcel<sup>‡</sup> aspect ratio and surface proximity by performing large-eddy simulations (LESs) of the motion of our free and surface cylinders,

using Das Atmosphärische Modell (DAM; Romps, 2008). DAM is fully compressible and relies on implicit LES (Margolin *et al.*, 2006) for subgrid-scale transport, so no explicit subgrid-scale turbulence scheme is used. We use a three-dimensional domain with doubly periodic boundary conditions in the horizontal, and take a neutrally stratified, dry environment with a temperature of 300 K at the lower boundary, where  $w$  and  $\beta$  are 0. The neutral stratification and surface temperature, along with an assumption of hydrostatic balance, are sufficient to determine the environmental density profile  $\bar{\rho}(z)$ . For given cylinder parameters  $D$  (which we vary) and  $H$  (which we fix at 1000 m), the domain width and height must be taken large enough to sufficiently approximate the horizontally infinite and vertically (half) infinite boundary conditions of the free (surface) cylinders. Since the scale height of  $p_{\beta}$  scales with  $D$  when  $D/H > 1$  (Appendix), and since we must leave room for our cylinders to rise, we take the domain height  $z_{\text{top}} = \max(2D, 6H)$  for free cylinders and  $z_{\text{top}} = \max(D, 4H)$  for surface cylinders. We take the domain width to be  $6.4D$ . This is sufficient to ensure only small<sup>§</sup> differences between the idealized analytical and finite-domain numerical profiles of  $\beta/B_0$ .

Our density field is

$$\rho(\mathbf{x}) = \bar{\rho}(z) - \frac{\bar{\rho}(z_{\text{cm}})}{300} \quad \text{for } r < D/2, |z - z_{\text{cm}}| < H/2,$$

with  $\rho = \bar{\rho}(z)$  everywhere else. The centre heights  $z_{\text{cm}}$  are  $z_{\text{top}}/2$  for the free cylinder and  $H/2$  for the surface cylinder. The grid spacings are  $dx = dy = D/40$  and  $dz = \min(dx, H/20)$ . The adaptive time step is set to a maximum of  $dz/(10 \text{ m s}^{-1})$  to satisfy the CFL condition (Durrant, 2010) for velocities up to at least  $\sim 10 \text{ m s}^{-1}$ .

The cylinders are initialized with a purity tracer field  $q_{\text{purity}}$  which is set to 1 inside the cylinder and 0 outside, and is advected passively by the flow. For each time  $t$ , we diagnose the cylinder's centre of mass  $z$ -coordinate as

$$z_{\text{cm}}(t) \equiv \frac{\int \int \int d^3\mathbf{x} z q(\mathbf{x}, t) \rho(\mathbf{x}, t)}{\int \int \int d^3\mathbf{x} q(\mathbf{x}, t) \rho(\mathbf{x}, t)},$$

where the integrals are taken over the whole model domain. To get a sense of how these parcels evolve, the  $q_{\text{purity}}$  field, along with  $z_{\text{cm}}(t)$ , is plotted at 3 min intervals for the  $D = 1000$  m free cylinder in Figure 7.

Next, we plot the trajectories  $z_{\text{cm}}(t) - z_{\text{cm}}(0)$  for free and surface cylinders in Figure 8. We take  $D = 200, 1000$ , and  $5000$  m, so that  $D/H = 1/5, 1$ , and  $5$ , just as in Figures 3 and 6. Figure 8 shows that the  $z_{\text{cm}}(t)$  trajectories indeed exhibit the expected dependence of effective buoyancy on aspect ratio. The effect of the surface is not noticeable for  $D/H = 1/5$  and  $1$ , but is noticeable for  $D/H = 5$ ; this is consistent with Figure 4, and

<sup>‡</sup>In this section we will continue to refer to our cylinders as ‘parcels’, even though the heterogeneity they develop over time violates the strict definition of a parcel as a homogenous entity.

<sup>§</sup>More specifically, the difference between the analytical and numerical profiles of  $\beta/B_0$  never exceeds 0.04, with the relative error in in-parcel acceleration (the quantity we care about) never exceeding 5% at a given height for a given case.

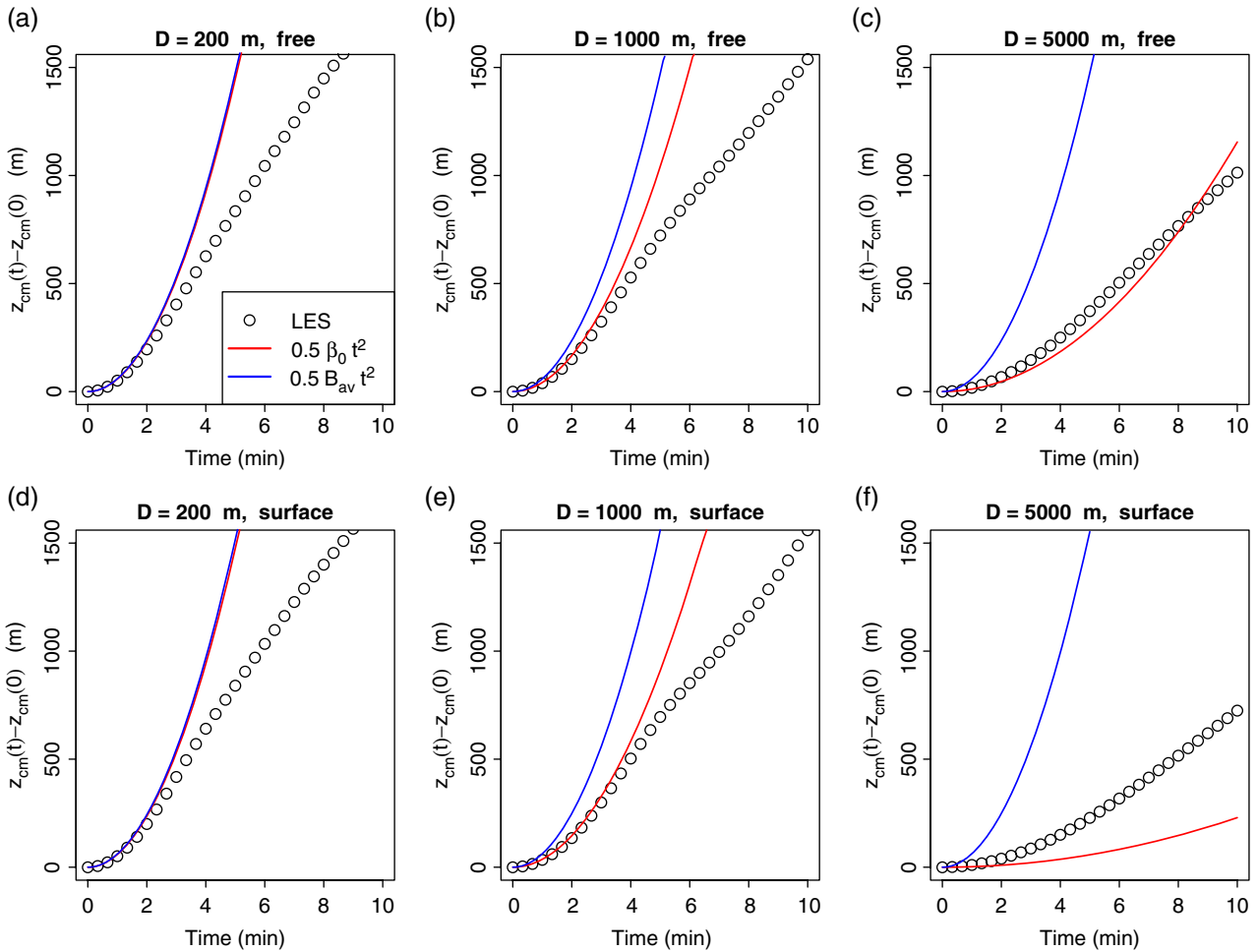


**Figure 8.** Diagnosed position of cylinder centre-of-mass  $z_{cm}(t)$  (open black circles) for our cylindrical density anomalies with  $H = 1000$  m and  $D =$  (a,d) 200 m, (b,e) 1000 m, and (c,f) 5000 m, as simulated by LES. The decreased acceleration with increasing aspect ratio is clear, especially when  $D/H \gtrsim 1$  and for the surface cylinder in particular. The blue line shows the Archimedean buoyancy estimate  $z_B(t)$  from Eq. (27), which for the skinny cylinders agrees with the LES at early times, but cannot capture the initial acceleration of the wider cylinders. The red line shows the effective buoyancy estimate  $z_\beta(t)$  from Eq. (28), which fares better in capturing the parcel’s initial acceleration for both free and surface cylinders, except for the  $D/H = 5$  cylinders. See the text for further discussion.

suggests that the effect of the surface becomes significant when  $D/H \gtrsim 1$ .

Figure 8 thus qualitatively confirms the physics presented in sections 3 and 4. Can the formulae (14) and (23) derived in those sections be of any quantitative use? And how do they compare with the naive predictions of the Archimedean buoyancy? Let us take a first stab at this by focusing on the initial acceleration of our cylinders. The Archimedean estimate for this is simply the average initial Archimedean buoyancy  $B_{av}$  ( $B$  is not exactly constant throughout the cylinder, due to small variations in  $\bar{\rho}(z)$ ), and so we plot the curve

$$z_B(t) \equiv 0.5 B_{av} t^2 \tag{27}$$

in blue for each panel of Figure 8. For the  $D/H = 1/5$  cylinders,  $z_B(t)$  matches  $z_{cm}(t)$  quite well for early times ( $t < 2$  to 3 min), and thus the Archimedean buoyancy is a good approximation to the initial acceleration of these parcels. As aspect ratio increases, though, there is a growing discrepancy between the initial accelerations of  $z_B(t)$  and  $z_{cm}(t)$  which is most pronounced for the surface cylinder. This is no surprise, though, as  $B_{av}$  is insensitive to aspect ratio and surface proximity; indeed, the curves  $z_B(t)$  are virtually identical for all six cases.

Let us now turn to the effective buoyancy  $\beta$ . By its very definition (4) and the fact that our simulated atmosphere is initially motionless, we know that the average  $\beta_{av}$  of  $\beta$  over the cylinder must equal the initial acceleration of  $z_{cm}(t)$ . The question, then, is to what degree the expressions (14) and (23), which strictly speaking only describe the centre of the cylinder, approximate  $\beta_{av}$ . To get a sense of this, we plot the

trajectories

$$z_\beta(t) \equiv 0.5 \beta_0 t^2, \tag{28}$$

where  $\beta_0$  is just given by Eqs (14) and (23) for the free and surface cases, respectively, against the diagnosed  $z_{cm}(t)$  in Figure 8. For  $D/H = 1/5$  the curves  $z_B(t)$  and  $z_\beta(t)$  are virtually identical, as one would expect, and both capture the initial acceleration of  $z_{cm}(t)$ . For  $D/H = 1$ ,  $z_\beta(t)$  captures the diagnosed initial acceleration whereas  $z_B(t)$  does not. For  $D/H = 5$ ,  $z_\beta(t)$  underestimates the initial acceleration quite significantly. This is because our uniform density anomalies with step function discontinuities feature a  $\beta$  that actually *increases* with  $r$  up to the cylinder’s edge at  $r = D/2$ , since that is where the singular source for  $\beta$  is located in the Poisson equations (12) and (21). For  $D/H \lesssim 1$ , these radial variations in  $\beta$  are small and so Eqs (14) and (23) are nonetheless good approximations to the average  $\beta$ , but for  $D/H > 1$  this is no longer true, and Eqs (14) and (23) underestimate the cylinder’s average  $\beta$ . This can also be seen in in Figure 9(a,c), where the curves (Eqs (14) and (23)) are overlain on  $\beta_{av}/B_{av}$  computed numerically for free and surface cylinders with  $H = 1000$  m and various  $D$ . In the next section we will come back to this figure, and discuss whether Eqs (14) and (23) can be of quantitative use when  $D/H > 1$ .

As a final aside, we should comment on the over-prediction of  $z_{cm}(t)$  by  $z_\beta(t)$  at later times ( $t > 3$  min) for the  $D/H \lesssim 1$  cases, where there is actually good initial agreement. Once a parcel begins to move, it experiences an internal circulation which may change its shape as well as entrain environmental air (Figure 7), both of which will reduce its effective buoyancy. Furthermore, we

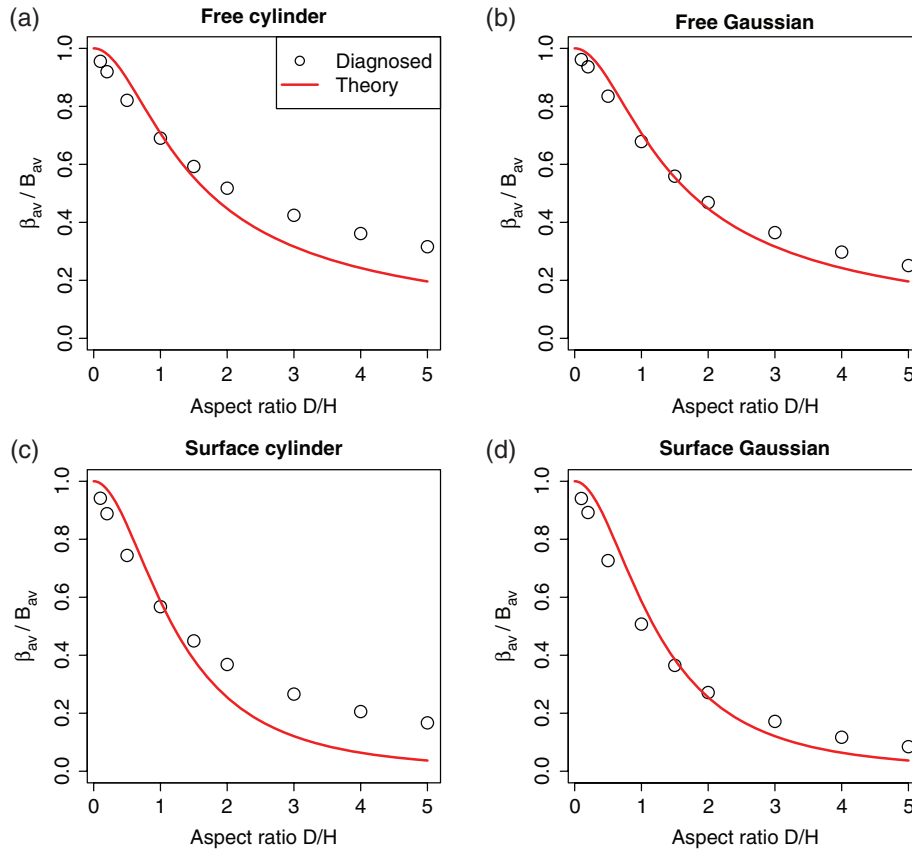


**Figure 9.** Comparison of the analytical expressions Eqs (14) and (23) with numerically diagnosed values of  $\beta_{av}/B_{av}$  for (a) free and (c) surface cylinders, and (b) free and (d) surface Gaussian bubbles of the form Eq. (3), with  $H = 1000$  m and various  $D$ . Our formulae rather significantly underestimate  $\beta_{av}/B_{av}$  for large-aspect-ratio cylinders, but give better agreement for large-aspect-ratio Gaussian bubbles.

expect drag forces to kick in and eventually balance any buoyant accelerations (Romps and Charn, 2015; Romps and Öktem, 2015), yielding a terminal velocity rather than continuing acceleration. Such a balance between buoyancy and drag at later times seems consistent with the diagnosed  $z_{cm}(t)$  in Figure 8, and would also contribute to an overestimation of  $z_{cm}(t)$  by  $z_{\beta}(t)$ .

## 6. Summary and discussion

We summarize our results as follows:

- The effective buoyancy of a fluid parcel depends on aspect ratio and surface proximity, as expressed in Eqs (13) and (22) and depicted in Figure 4.
- These effects can be understood in terms of the buoyancy pressure  $p_{\beta}$ , of which  $\beta$  is essentially just the vertical gradient.
- These effects indeed manifest in parcel motion as simulated by LES.

Many questions and potential applications remain, of course. An obvious first question is: what determines the aspect ratio of real convecting elements in the atmosphere? Our work here quantifies the well-known advantage that skinny parcels have over squat parcels in convecting. But a parcel that is too skinny will likely suffer too much dilution from entrainment to convect very far, and so the aspect ratio of real clouds is most likely determined by a balance between effective buoyancy and entrainment. Settling this question quantitatively, however, would require a more solid understanding of how entrainment varies with aspect ratio (de Rooy *et al.*, 2013).

Another obvious follow-up question is: to what extent do Eqs (14) and (23), which even for our highly idealized uniform cylinders only capture  $\beta_{av}$  for  $D/H \lesssim 1$ , apply to real convective clouds, which have highly heterogeneous density distributions and irregular shapes? Interestingly, if we consider slightly less artificial

density distributions such as Gaussian bubbles of the form (3), then we no longer get an increase of  $\beta$  with  $r$  (Figure 1), and Eqs (14) and (23) give a better approximation of  $\beta_{av}/B_{av}$ , as shown in Figure 9(b,d). Thus, we may hold out some hope that our analytical expressions apply to more realistic convection. However, a comparison with density distributions derived from (say) cloud-resolving simulations would be necessary to confirm this.

We should note here that Eq. (14) is not the only published candidate for  $\beta$  as a function of aspect ratio. Recently, Nugent and Smith (2014) calculated  $\beta$  for a horizontally infinite slab of height  $H$  with sinusoidal density variations in  $x$  and  $y$ , and found that for such density distributions

$$\beta = B \{1 - \exp(-H/D)\}, \quad (29)$$

where  $D = 2/\sqrt{k^2 + l^2}$  is an effective diameter and  $k, l$  are the horizontal wavenumbers of the distribution. This curve is plotted in Figure 4 in light grey, and matches quite closely the curve of Eq. (14). Equation (29) can also be obtained by integrating a uniform buoyancy profile of height  $H$  and centre-of-mass height  $z_{cm} \rightarrow \infty$  against the Green's function in Eq. (15) of Pauluis and Garner (2006). That article also touches upon the effect of the surface, and emphasizes the application of formulae such as their Eqs (18) and (21) (analogous to our Eqs (14) and (23)) to understanding the transition from hydrostatic to non-hydrostatic regimes in numerical modelling. In this regard, note that Eq. (23) tells us that a grid-point surface plume of height 1 km in a 'convection-permitting' model of horizontal resolution 4 km (the threshold identified in the recent review by Prein *et al.* (2015)) should experience a roughly order-of-magnitude reduction in acceleration from the Archimedean value.

Finally, we note that the basic physics investigated here, namely the effect of environmental inertia on an accelerating parcel, is well known in the fluid dynamics literature as the 'virtual mass' or 'induced mass' effect (e.g. Batchelor, 2000; Falkovich, 2011).

This effect is usually incorporated into parametrizations of the vertical velocity equation, which often take the form (de Roode *et al.*, 2012)

$$\frac{dw}{dt} = aB - b\epsilon w^2, \quad (30)$$

where  $a$  and  $b$  are dimensionless;  $a$  is often referred to as a ‘virtual mass coefficient’ (e.g. Bretherton *et al.*, 2004), and  $\epsilon$  is an entrainment rate (units  $\text{m}^{-1}$ ). The  $-\epsilon w^2$  expression captures the effect of entrainment (mixing) drag, and  $b$  accounts for other types of drag such as form drag and wave drag, all of which are expected to be proportional to  $w^2$ . Before relating our results to such a parametrization, we should re-arrange Eq. (30) as it is unsatisfactory on two grounds. First, since  $b$  multiplies  $\epsilon$ , it introduces a spurious connection between (say) form drag and entrainment. Second, *any* force (not just buoyancy) will induce a back-reaction from the environment, and so the virtual mass coefficient  $a$  should multiply the drag term as well (assuming that the spatial distribution of buoyancy and drag forces is identical, so that we may use the same virtual mass coefficient). This suggests a drag term of the form  $a\{c_d A/2V + \epsilon\}w^2$ , where  $A$  is the projected area of the parcel,  $V$  is its volume, and  $c_d$  is a drag coefficient representing form and wave drag. Equation (30) can then be re-written as

$$\frac{1}{a} \frac{dw}{dt} = B - \left( \frac{c_d A}{2V} + \epsilon \right) w^2, \quad (31)$$

which combined with the definition (4) yields

$$a = \beta/B.$$

Thus, our results (14) and (23) are just highly idealized calculations of the virtual mass coefficient  $a$ . Furthermore, they show that this coefficient depends on surface proximity.

Other analytical calculations of virtual mass coefficients exist in the fluid dynamics literature, but are often for foreign objects such as gas bubbles or solid spheres accelerating through a fluid (e.g. Batchelor, 2000; Falkovich, 2011). Our case differs from that treated in textbooks in that the mass we are considering is part of the fluid, and so may accelerate non-uniformly and develop an internal circulation (as seen in Figure 7). Mathematically, the difference is that we have no boundary condition on the environmental fluid velocity at the parcel’s edge, as there would be for a solid body. However, it could be of theoretical and perhaps practical interest to compare our expressions (14) and (23) to analogous expressions for solid bodies of similar geometries, such as the results of Brumley *et al.* (2010). That there may be some connection is suggested by the special case of a sphere. To approximate this case we set  $D = H$  in Eq. (14), which yields an acceleration of  $B_0/\sqrt{2} \approx 0.71B_0$ ; this is quite close to the solid-body value of  $2B_0/3$ , typically derived by other means (Falkovich, 2011).

## Appendix

### The invariance of $p_\beta/p_\beta(0)$ in the $D/H \gg 1$ limit

Consider the free cylinder’s buoyancy distribution, Eq. (11). Setting  $\mathbf{x}' = \mathbf{x}/D$  we can write this as

$$B(\mathbf{x}') = B_0 \mathcal{H}\left(\frac{1}{2} - r'\right) \mathcal{H}\left(z' + \frac{H}{2D}\right) \mathcal{H}\left(\frac{H}{2D} - z'\right).$$

In the  $D/H \gg 1$  limit, the product of the last two Heaviside functions becomes a delta function  $(H/D)\delta(z')$ , i.e. the cylinder becomes a horizontal ‘line source’ in the primed coordinates. Feeding this  $B$  field into the definition of  $p_{\text{hyd}}$  and employing Eqs (17) and (18) yields

$$-\nabla'^2 \left( \frac{p_\beta}{p_\beta(0)} \right) = -2\mathcal{H}(-z') \nabla_h'^2 \mathcal{H}\left(\frac{1}{2} - r'\right). \quad (A1)$$

This tells us that  $p_\beta/p_\beta(0)$  is an invariant function of  $\mathbf{x}'$ , insensitive to changes in  $H$  and  $D$  within the  $D/H \gg 1$  regime. In particular, we conclude that  $p_\beta/p_\beta(0)$  will decay along the  $z$ -axis to a given fraction of itself at a fixed  $z' = z/D$ , and hence this ‘scale height’ of  $p_\beta$  scales with  $D$ .

Repeating this exercise but for the surface cylinder (or for a cylinder close to the surface, i.e.  $z_{\text{cm}} \ll D$ ) yields an expression identical to Eq. (A1), except with the replacement  $\mathcal{H}(-z') \rightarrow \delta(z')$ . In this case, we conclude that both the scale height as well as the height  $z_{\text{max}}$  of maximum  $\beta$  scale with  $D$ .

## Acknowledgements

This work was supported by the Scientific Discovery through Advanced Computing (SciDAC) program funded by the US Department of Energy Office of Advanced Scientific Computing Research and Office of Biological and Environmental Research under contract No. DE-AC02-05CH11231. This research used resources of the National Energy Research Scientific Computing Center, a DOE Office of Science User Facility supported by the Office of Science of the US Department of Energy, and resources of the Extreme Science and Engineering Discovery Environment (XSEDE), which is supported by National Science Foundation grant number ACI-1053575. We thank two anonymous referees for detailed and constructive reviews, and NJ thanks Wolfgang Langhans for discussions.

## References

- Batchelor GK. 2000. *An Introduction to Fluid Dynamics*. Cambridge University Press: Cambridge, UK.
- Bretherton CS, McCaa JR, Grenier H. 2004. A new parameterization for shallow cumulus convection and its application to marine subtropical cloud-topped boundary layers. Part I: Description and 1D results. *Mon. Weather Rev.* **132**: 864–882.
- Brumley DR, Willcox M, Sader JE. 2010. Oscillation of cylinders of rectangular cross-section immersed in fluid. *Phys. Fluids* **22**: 052001, doi: 10.1063/1.3397926.
- Das P. 1979. A non-Archimedean approach to the equations of convection dynamics. *J. Atmos. Sci.* **36**: 2183–2190.
- Davies-Jones R. 2003. An expression for effective buoyancy in surroundings with horizontal density gradients. *J. Atmos. Sci.* **60**: 2922–2925.
- Doswell Ca, Markowski PM. 2004. Is buoyancy a relative quantity? *Mon. Weather Rev.* **132**: 853–863.
- Durran DR. 2010. *Numerical Methods for Fluid Dynamics: With Applications to Geophysics*. Springer: Berlin and Heidelberg, Germany.
- Emanuel KA. 1994. *Atmospheric Convection*. Oxford University Press: New York, NY.
- Falkovich G. 2011. *Fluid Mechanics: A Short Course for Physicists*. Cambridge University Press: Cambridge, UK.
- Griffiths DJ. 2013. *Introduction to Electrodynamics*. Pearson Education: Boston.
- Houze RA Jr. 2014. *Cloud Dynamics*. Academic Press: Waltham, MA.
- Jeevanjee N, Roms DM. 2015. Effective buoyancy, inertial pressure, and the mechanical generation of boundary-layer mass flux by cold pools. *J. Atmos. Sci.* **72**: 3199–3213.
- Krueger SK, McLean GT, Fu Q. 1996. Numerical simulation of the stratus-to-cumulus transition in the subtropical marine boundary layer. Part II: Boundary-layer circulation. *Oceanogr. Lit. Rev.* **3**: 228.
- Margolin LG, Rider WJ, Grinstein FF. 2006. Modeling turbulent flow with implicit LES. *J. Turbul.* **7**: N15, doi: 10.1080/14685240500331595.
- Markowski P, Richardson Y. 2011. *Mesoscale Meteorology in Midlatitudes*. John Wiley and Sons: Chichester, UK.
- Nugent AD, Smith RB. 2014. Initiating moist convection in an inhomogeneous layer by uniform ascent. *J. Atmos. Sci.* **71**: 4597–4610.
- Pauluis O, Garner S. 2006. Sensitivity of radiative–convective equilibrium simulations to horizontal resolution. *J. Atmos. Sci.* **63**: 1910–1923.
- Prein AF, Langhans W, Fossler G, Ferrone A, Ban N, Goergen K, Keller M, Tölle M, Gutjahr O, Feser F, Brisson E, Kollet S, Schmidli J, van Lipzig NPM, Leung R. 2015. A review on regional convection-permitting climate modeling: demonstrations, prospects, and challenges. *Rev. Geophys.* **53**: 323–361, doi: 10.1002/2014RG000475.
- Roms DM. 2008. The dry-entropy budget of a moist atmosphere. *J. Atmos. Sci.* **65**: 3779–3799.
- Roms DM, Charn AB. 2015. Sticky thermals: evidence for a dominant balance between buoyancy and drag in cloud updrafts. *J. Atmos. Sci.* **72**: 2890–2901.
- Roms DM, Öktem R. 2015. Stereo photogrammetry reveals substantial drag on cloud thermals. *Geophys. Res. Lett.* **42**: 5051–5057, doi: 10.1002/2015GL064009.

- de Roode SR, Siebesma AP, Jonker HJJ, de Voogd Y. 2012. Parameterization of the vertical velocity equation for shallow cumulus clouds. *Mon. Weather Rev.* **140**: 2424–2436.
- de Rooy WC, Bechtold P, Fröhlich K, Hohenegger C, Jonker H, Mironov D, Pier Siebesma A, Teixeira J, Yano JI. 2013. Entrainment and detrainment in cumulus convection: an overview. *Q. J. R. Meteorol. Soc.* **139**: 1–19.
- Torri G, Kuang Z, Tian Y. 2015. Mechanisms for convection triggering by cold pools. *Geophys. Res. Lett.* **42**: 1943–1950, doi: 10.1002/2015GL063227.
- Xu KM, Randall DA. 2001. Updraft and downdraft statistics of simulated tropical and midlatitude cumulus convection. *J. Atmos. Sci.* **58**: 1630–1649.
- Yau MK. 1979. Perturbation pressure and cumulus convection. *J. Atmos. Sci.* **36**: 690–694.